

A ballistic model for a precessing and orbiting jet with a time-dependent ejection velocity

Pablo F. Velázquez,^{1*} Alejandro C. Raga,¹ Jorge Cantó,² E. Matias Schneiter^{3†} and Angels Riera^{4,5}

¹*Instituto de Ciencias Nucleares, Universidad Nacional Autónoma de México, México D.F., México*

²*Instituto de Astronomía, Universidad Nacional Autónoma de México, Apdo. Postal 70-242, CP: 04510 D.F., México*

³*Instituto de Astronomía Teórica y Experimental, Córdoba, Argentina*

⁴*Departament de Física i Enginyeria Nuclear, EUETIB, Universitat Politècnica de Catalunya, Compte d'Urgell 187, 08036 Barcelona, Spain*

⁵*Departament d'Astronomia i Meteorologia, Universitat de Barcelona, Av. Diagonal 647, 08028 Barcelona, Spain*

Accepted 2012 October 2. Received 2012 September 5

ABSTRACT

We have found that the ballistic trajectory of a precessing, orbiting and time-dependent velocity jet has a semi-analytical solution. Bipolar, multipolar and S-like morphologies, which are observed in young protoplanetary and planetary nebula (PPN and PN, respectively), can be reproduced by setting different values for the ratio between dynamical time and precession periods, the ratio between the precession and orbital periods, and the jet velocity variability period. We have also computed numerical simulations and find a good agreement with the semi-analytical solution for a jet 10^3 times denser than the surrounding environment.

Key words: hydrodynamics – methods: analytical – methods: numerical – ISM: jets and outflows – planetary nebulae: general.

1 INTRODUCTION

Collimated outflows or jets ejected by young stars or by the central sources of protoplanetary and planetary nebulae (PPNe and PNe, respectively) can be considered as ballistic if the jet material is much denser than the gas of the circumstellar medium in which the jet propagates. A ballistic model is a good tool for providing restrictions for the parameters employed for describing the morphologies observed in these astrophysical objects.

Masciadri & Raga (2002) carried out an analytical and numerical study of jets launched from a source which follows a circular orbit. They found that this model produces global mirror-like morphologies. The case of a jet launched from a source in an elliptical orbit was explored by González & Raga (2004).

A combination of a precessing and orbiting jet (from a source tracing a circular orbit) was analysed by Raga et al. (2009). They found that the ballistic trajectory of the jet material has an analytical solution, and show that the effects of the orbital motion on the final ballistic trajectory are observed at a distance $D_o = v_j \tau_o$ from the jet source. If the orbital period τ_o is lower than the precession period τ_p , a point-symmetric morphology is observed farther away from the central source (due to the precession).

A possible mechanism invoked for explaining the bipolar and multipolar morphologies exhibited by PPNe and young PNe is the presence of a binary system (Bond, Liller & Mannery 1978; Livio, Salzman & Shaviv 1979; Soker & Livio 1994). One of the components of the binary system forms an accretion disc (with material from the companion star) and launches a jet (perpendicular to this disc). The companion star produces a torque on the accretion disc which generates a retrograde precession of the disc/jet system (Terquem et al. 1999). Additionally, a variability of the ejection velocity can be produced if the binary system follows an elliptical orbit, as reported by Witt et al. (2009). Velázquez et al. (2012) considered these elements (binary system and a jet with a time-dependent ejection velocity) and modelled multipolar PPN by means of 3D hydrodynamical simulations.

In this work, we follow the ideas of Masciadri & Raga (2002), González & Raga (2004) and Raga et al. (2009) and find that the case of a precessing, orbiting and time-dependent ejection velocity jet has a semi-analytical solution for its ballistic trajectory (the solution is analytical for the case of a circular orbit). We then compare this ballistic model with results obtained from 3D numerical simulations, which were carried out with the Yguazú-a code. This work is organized as follows: in Section 2 we present the ballistic model, and in Section 3 we give the initial setup of both the ballistic solution and the numerical simulations. The results are shown in Section 4, and finally we present our conclusions in Section 5.

* E-mail: pablo@nucleares.unam.mx

† Member of the Carrera del Investigador Científico, CONICET, Argentina.

2 BALLISTIC MODEL

As was previously mentioned, the jet material approximately has a ballistic motion if its density is much larger than the density of the surrounding medium. We assume that the jet has a time-dependent ejection velocity $v_j(\tau)$. The jet source moves in an elliptical orbit (we also consider the particular case of a circular orbit), and the ejection direction precesses, describing a cone around the orbital (z) axis, with a half-opening angle α . The orbital motion lies on the xy plane, and the precession of the disc+jet system is retrograde with respect to the orbital motion (see Terquem et al. 1999).

The (x, y, z) components of the ejection velocity at time τ , considering both orbital and precession effects, are

$$v_x(\tau) = v_j(\tau) \sin \alpha \cos(-\omega_p \tau + \phi_0) + v_{ox}(\tau) \quad (1)$$

$$v_y(\tau) = v_j(\tau) \sin \alpha \sin(-\omega_p \tau + \phi_0) + v_{oy}(\tau) \quad (2)$$

$$v_z(\tau) = v_j(\tau) \cos \alpha, \quad (3)$$

where ω_p is the precession angular frequency, ϕ_0 is an initial phase and $v_j(\tau)$ is the time-dependent ejection velocity for which we consider a periodic variability of the form

$$v_j(\tau) = v_{j0}[1 + \Delta v \cos(\omega_o \tau + \delta_0)], \quad (4)$$

where ω_o is the orbital frequency (based on Witt et al 2009, we assume the same frequency for the orbital motion and jet velocity variability), v_{j0} the mean jet velocity, Δv the half-amplitude (in units of v_{j0}) and δ_0 the initial phase of the ejection velocity variability. In equations (1) and (2), v_{ox} and v_{oy} are the x - and y components of the orbital speed. For a circular orbit, these velocity components are

$$v_{ox} = -v_o \sin(\omega_o \tau + \gamma_0); \quad v_{oy} = v_o \cos(\omega_o \tau + \gamma_0), \quad (5)$$

where γ_0 is a phase.

We now determine the locus of the ejected material at time t . This material has been ejected at times $t > \tau$, with the velocity components given by equations (1)–(3). At time t , the position of the gas ejected at a time τ is given by

$$(x, y, z) = (t - \tau)(v_x, v_y, v_z). \quad (6)$$

Let us call D the distance to the ejected material farthest away from the source, along the symmetry axis of the object. Then, if we set ‘now’ as $t = 0$, the gas located at a distance D was launched at a time $\tau = -\tau_d$, with $\tau_d = D/(v_{\max} \cos \alpha)$ being the dynamical time of the material at a distance D from the source, and $v_{\max} = v_{j0}(1 + \Delta v)$. For $\tau = -\tau_d$ the precession, orbital and jet velocity variability phases are

$$\omega_p \tau_d + \phi_0 = f_0 \quad (7)$$

$$-\omega_o \tau_d + \gamma_0 = g_0 \quad (8)$$

$$-\omega_o \tau_d + \delta_0 = d_0, \quad (9)$$

respectively. Assuming $g_0 = 0$, i.e. at $\tau = -\tau_d$ the binary system is passing through its periastron, and combining equations (7)–(9) with equations (6), we obtain

$$x = -\tau v_j(\tau) \sin \alpha \cos[-\omega_p(\tau + \tau_d) + f_0] + \tau v_o \sin[\omega_o(\tau + \tau_d)] \quad (10)$$

$$y = -\tau v_j(\tau) \sin \alpha \sin[-\omega_p(\tau + \tau_d) + f_0] - \tau v_o \cos[\omega_o(\tau + \tau_d)] \quad (11)$$

$$z = -\tau v_j(\tau) \cos \alpha, \quad (12)$$

where $v_j(\tau) = v_{j0}\{1 + \Delta v \cos[\omega_o(\tau + \tau_d) + d_0]\}$.

The following step is to write equations (10)–(12) in a dimensionless form, which can be done by dividing both sides of equations (10)–(12) by D and writing τ as $-\tau' \tau_d$ (where τ' is a dimensionless time). Also we set $\tau_d = p \tau_p$ and $\tau_p = q \tau_o$, where p and q are two dimensionless parameters (following Velázquez et al. 2012).

The q parameter allows us to estimate the mass ratio m_2/m_1 between the two components of the binary system, considering the work of Terquem et al. (1999). Choosing a value for m_1 or m_2 , the orbital radius and velocity can be calculated (by using Kepler’s third law). Then, the dimensionless form of equations (10)–(12) is

$$x' = \pm \tau' v'_j(\tau') \tan \alpha \cos[\omega'_p(\tau' - 1) + f_0] + \tau' v'_o \sin[\omega'_o(\tau' - 1)] \quad (13)$$

$$y' = \pm \tau' v'_j(\tau') \tan \alpha \sin[\omega'_p(\tau' - 1) + f_0] + \tau' v'_o \cos[\omega'_o(\tau' - 1)] \quad (14)$$

$$z' = \pm \tau' v'_j(\tau'), \quad (15)$$

with $v'_j(\tau') = 1 + \Delta v \cos[\omega'_o(\tau' - 1) - d_0]/(1 + \Delta v)$ and $v'_o = v_o/(v_{\max} \cos \alpha)$. $\omega'_p = \omega_p \tau_d = 2\pi p$ and $\omega'_o = \omega_o \tau_d = 2\pi pq$ are the dimensionless precession and orbital frequencies, respectively. The $+$ ($-$) sign corresponds to the trajectory of the gas emitted by the jet (counterjet). The solution given by equations (13)–(15) is analytical.

For the case of an elliptical orbit with an eccentricity e and semi-major axis a , v_{ox} and v_{oy} have to be evaluated as follows. These velocities can be written as a function of the polar coordinates r and θ (and their derivatives), in the following way:

$$v_{ox} = \dot{r} \cos \theta - r \dot{\theta} \sin \theta, \quad (16)$$

$$v_{oy} = \dot{r} \sin \theta + r \dot{\theta} \cos \theta. \quad (17)$$

In order to obtain r and θ as a function of τ , it is necessary to take into account the orbital equation in polar coordinates:

$$r = \frac{a(1 - e^2)}{1 + e \cos \theta}. \quad (18)$$

Table 1. Models.

Models	Δv	p	q	ϵ	m_2/m_1	$\alpha(^{\circ})$	f_0	d_0
M1a	0.5	2	2	0.5	14.8	15.0	0.0	0.0
M1b	0.5	2	2	0.5	14.8	15.0	0.0	$-\pi/2$
M1c ^a	0.5	2	2	–	14.8	15.0	0.0	$-\pi/2$
M1d	0.5	2	2	0.0	33.9	15.0	0.0	$-\pi/2$
M2	0.5	2	3	0.5	8.6	30.0	0.0	0.0
M3	0.5	2	4	0.5	5.2	30.0	$\pi/4$	0.0
M4	0.5	2	1.5	0.75	5.5	5.0	$\pi/4$	0.0
M5	0.25	0.5	6.0	0.5	2.2	15.0	$\pi/4$	$-\pi/2$

^aModels M1c and M1b differ in that the former only considers precession motion.

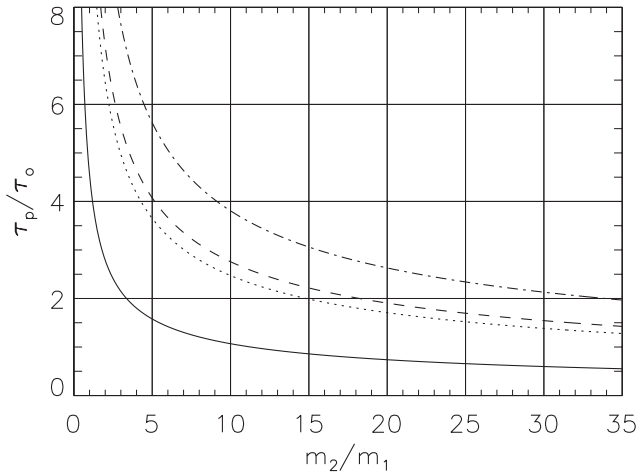


Figure 1. Plot of τ_p/τ_0 versus m_2/m_1 for different values of α and e listed in Table 1. The case for $\alpha = 5^\circ$ and $e = 0.75$ is displayed as a continuous line. The case for $\alpha = 15^\circ$ and $e = 0.5$ is shown as a dotted line. The curve for the case $\alpha = 30^\circ$ and $e = 0.5$ is traced as a dashed line, while the case for $\alpha = 15^\circ$ and $e = 0$ (circular orbit) is plotted as a dot-dashed line.

Introducing the eccentric anomaly E , this equation can be written as

$$r = a(1 - e \cos E), \tag{19}$$

with E being related to the polar angle θ by

$$\tan \frac{\theta}{2} = \left(\frac{1+e}{1-e} \right)^{1/2} \tan \frac{E}{2}. \tag{20}$$

The velocities \dot{r} and $\dot{\theta}$ can be obtained from equations (18)–(20), resulting in

$$\dot{\theta} = \left(\frac{1+e}{1-e} \right)^{1/2} \left[\frac{\cos(\theta/2)}{\cos(E/2)} \right]^2 \frac{\omega_0}{1 - e \cos E} \tag{21}$$

$$\dot{r} = \frac{ae \sin \theta (1 - e^2)}{(1 + e \cos \theta)^2} \dot{\theta}. \tag{22}$$

The next step is to obtain $E(\tau)$ from Kepler’s equation:

$$E - e \sin E = \omega_0 \tau + \gamma_0. \tag{23}$$

As in equation (8), for $\tau = -\tau_d$, γ_0 is chosen such that $-\omega_0 \tau_d + \gamma_0 = 0$. Writing the right-hand side of equation (23) in a dimensionless form, we have

$$E - e \sin E = \omega'_0(1 - \tau'). \tag{24}$$

In order to calculate v_{ox} and v_{oy} we then follow the following procedure:

- (a) we solve numerically equation (24) (i.e. by means of a Newton–Raphson method) in order to obtain $E(\tau)$, choosing as initial value $E(\tau) = \omega'_0$,
- (b) we introduce the resulting $E(\tau)$ into equation (19) and (20) to obtain $r(\tau)$ and $\theta(\tau)$,
- (c) we finally introduce equations (21) and (22) into equations (16) and (17).

We then obtain a dimensionless form for the trajectory, given by equations (10)–(12), for the elliptical orbit case:

$$\begin{aligned} x' &= \pm \tau' v'_j(\tau') \tan \alpha \cos[\omega'_p(\tau' - 1) + f_0] \\ &\quad - \tau' v'_{ox}(\tau') \end{aligned} \tag{25}$$

$$\begin{aligned} y' &= \pm \tau' v'_j(\tau') \tan \alpha \sin[\omega'_p(\tau' - 1) + f_0] \\ &\quad + \tau' v'_{oy}(\tau') \end{aligned} \tag{26}$$

$$z' = \pm \tau' v'_j(\tau'). \tag{27}$$

3 INITIAL SETUP

3.1 Semi-analytical ballistic model

Employing equations (25)–(27), we have traced several trajectories for the parameters of the models listed in Table 1. As mentioned above, the q parameter allows us to estimate the mass ratio m_2/m_1 between the components of the binary system. Employing equation (1) of Terquem et al. (1999), and choosing the values for e and α , we have calculated τ_p/τ_0 versus m_2/m_1 plots, which are displayed in Fig. 1. Using this figure, for each q value listed in Table 1, we can estimate its corresponding m_2/m_1 . We have set $m_1 = 0.5M_\odot$ for all models.

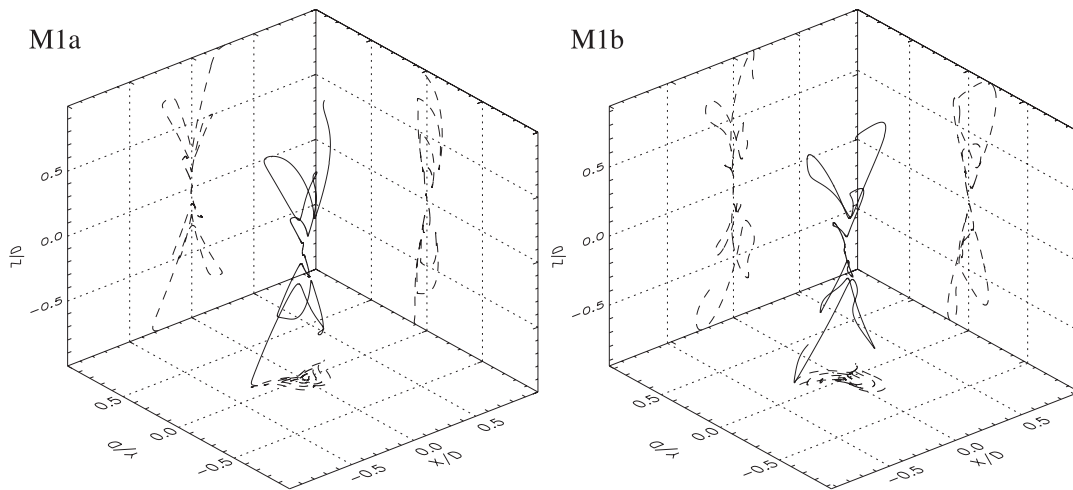


Figure 2. 3D ballistic trajectories corresponding to models M1a (left-hand panel) and M1b (right-hand panel). The projections of these trajectory on each three planes are plotted as dashed lines. The axes are given in dimensionless units.

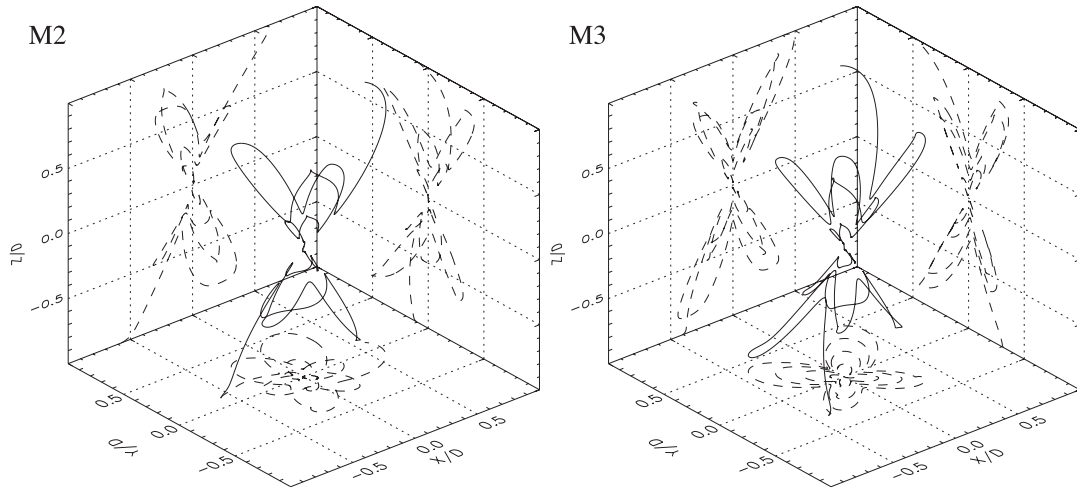


Figure 3. Same as Fig. 2 but for models M2 (left-hand panel) and M3 (right-hand panel).

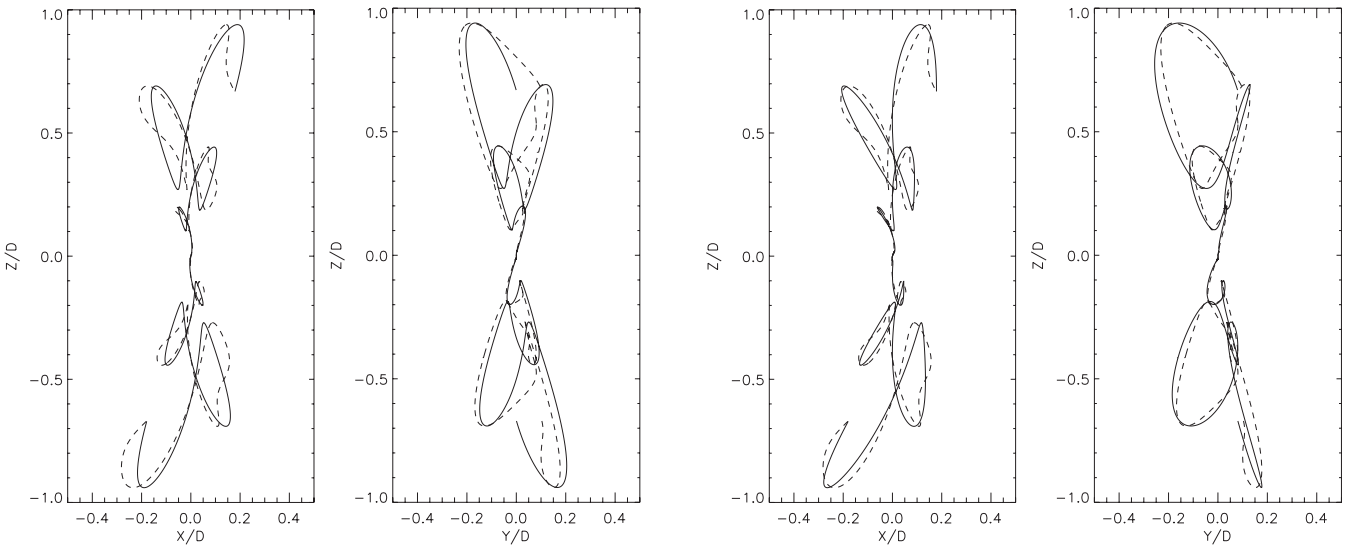


Figure 4. The left-hand panel shows a comparison between trajectories of model M1c (only precession, continuous line) and M1b (precession+orbital motion, dashed line) projected on the xz plane. The right-hand panel shows the yz projection of these trajectories. The axes are given in dimensionless units.

Figure 5. The left-hand panel (right-hand panel) shows a comparison between trajectories of models M1d (circular orbit, continuous line) and M1b (elliptical orbit, dashed line) projected on the xz plane (yz plane). Both axes are given in dimensionless units.

In these models, we have explored the effects of the orbital motion (circular and elliptical: models M1d and M1b, respectively) on the final locus traced by a jet with a time-dependent ejection velocity. Models M1b and M1c allow us to directly compare the cases with precession+orbital motion and with only precession. Also, we have calculated the jet loci obtained by setting the p and q parameters to non-integer values.

3.2 Numerical simulations

In order to compare the results obtained from the semi-analytical method described in the previous section, we also carried out 3D hydrodynamic simulations for some of the models of Table 1.

The 3D numerical simulations were performed with the YGUAZÚ-A hydrodynamical code (Raga et al. 2000), which integrates the gas dynamical equations with a second-order accurate scheme (in time

and space) using the ‘flux-vector splitting’ method of van Leer (1982) on a binary adaptive grid. A rate equation for neutral hydrogen is integrated together with the gas dynamic equations, and the radiative losses are included with a parametrized cooling function that depends on the density, temperature and hydrogen ionization fraction (Raga & Reipurth 2004). The resulting time-dependent cooling function is plotted in fig. 1 of Velázquez et al. (2011) for a gas parcel that cools at a constant (atom+ion) number density $n = 1 \text{ cm}^{-3}$.

A computational domain of $(1.25, 1.25, 2.5) \times 10^{17} \text{ cm}$ along the x -, y - and z axes (respectively) was employed. An adaptive Cartesian grid with five refinement levels was used, achieving a resolution of $\sim 4.9 \times 10^{14} \text{ cm}$ at the finest level, corresponding to $(256 \times 256 \times 512)$ pixels in a uniform grid.

At the centre of the computational domain, we impose a precessing, orbiting and time-dependent ejection velocity jet with a radius of $3.5 \times 10^{15} \text{ cm}$ and a length of $3 \times 10^{15} \text{ cm}$. Models M1a, M1b, M2, M3, M4 and M5 have been computed employing the

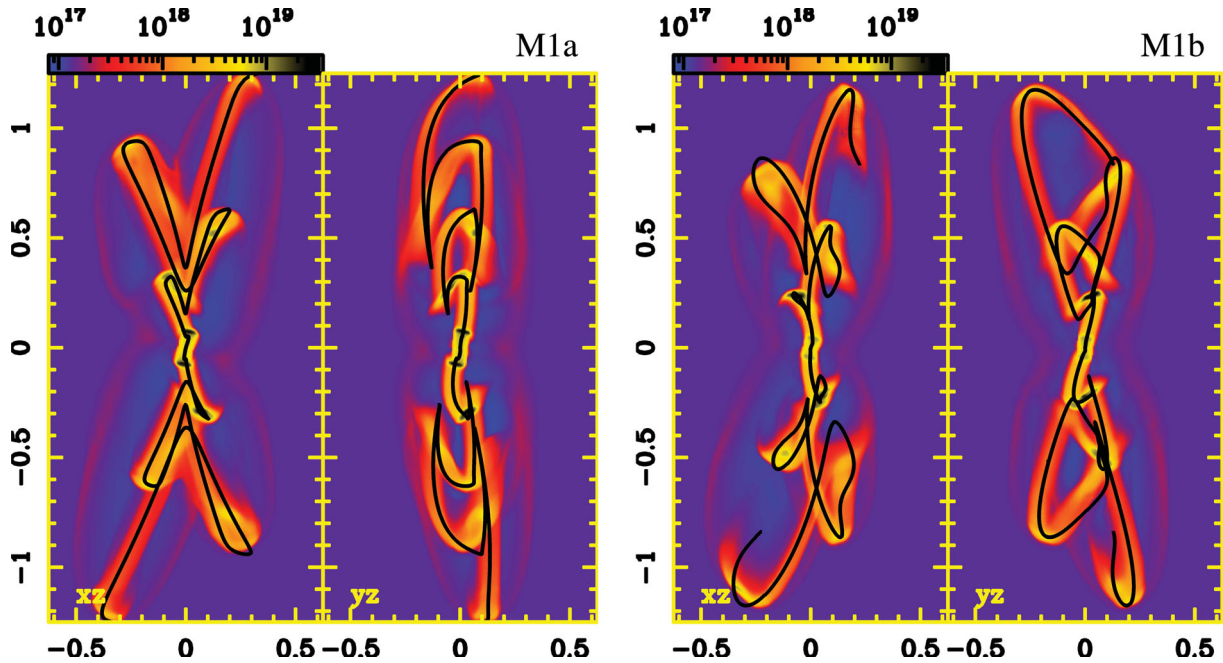


Figure 6. Left-hand panels: xz and yz projections of the column-density maps obtained for model M1a. Right-hand panels: the same but for model M1b. Vertical and horizontal axes are given in units of 10^{17} cm, while the logarithmic colour scale is given in cm^{-2} . The ballistic trajectories obtained for each model are overlaid in white continuous lines.

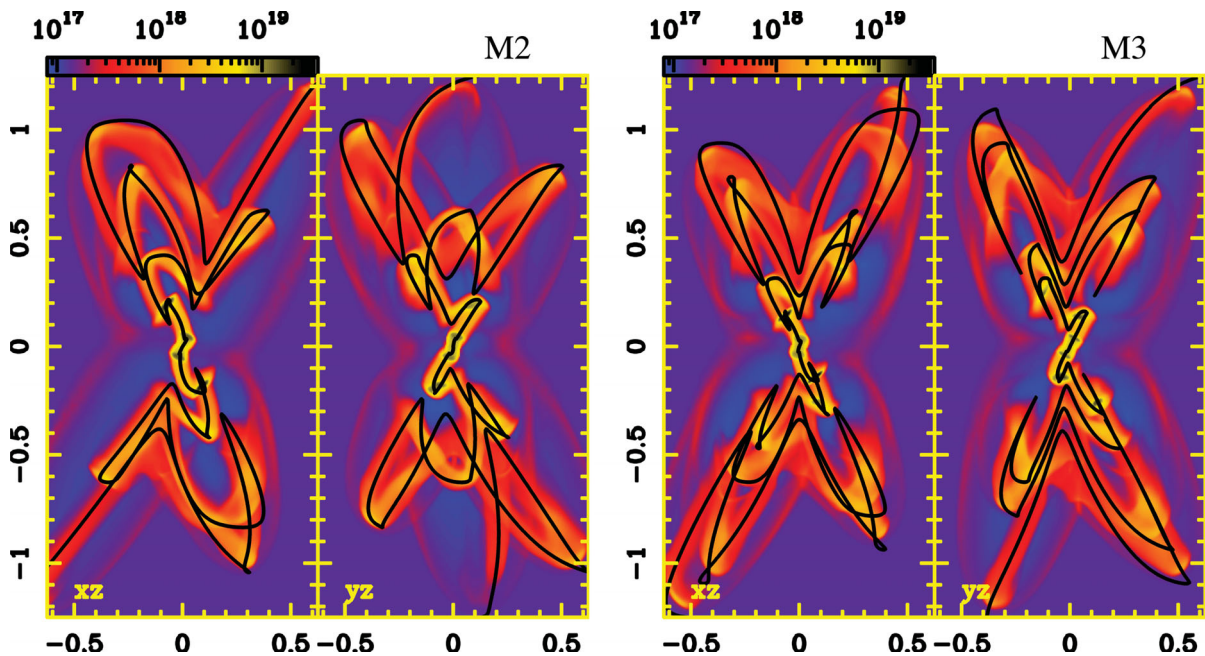


Figure 7. Same as Fig. 6 but left-hand panels showing the column-density maps for model M2, while right-hand panels corresponding to model M3.

parameters listed in Table 1. The initial number density of the jet was set to 10^3 cm^{-3} , and its mean velocity to 200 km s^{-1} . The jet material propagates into a circumstellar medium with a constant density of 1 cm^{-3} or 10 cm^{-3} , in order to compare the results with the predicted trajectories.

4 RESULTS

We obtained the ballistic trajectories for models with the parameters listed in Table 1.

Fig. 2 shows the 3D trajectories traced by models M1a (left) and M1b (right) with solid lines. The projections of the trajectories on the coordinate planes are shown in dashed lines. These models differ from each other in the initial phase of the jet velocity variability. In both models, the projected trajectory on the xz plane traces a point-symmetric quadrupolar shape, and this quadrupolar morphology becomes a bipolar structure for the yz projection of model M1a. In contrast, the yz projection of model M1b shows a wide and well-developed upper lobe and a pair of bottom lobes.

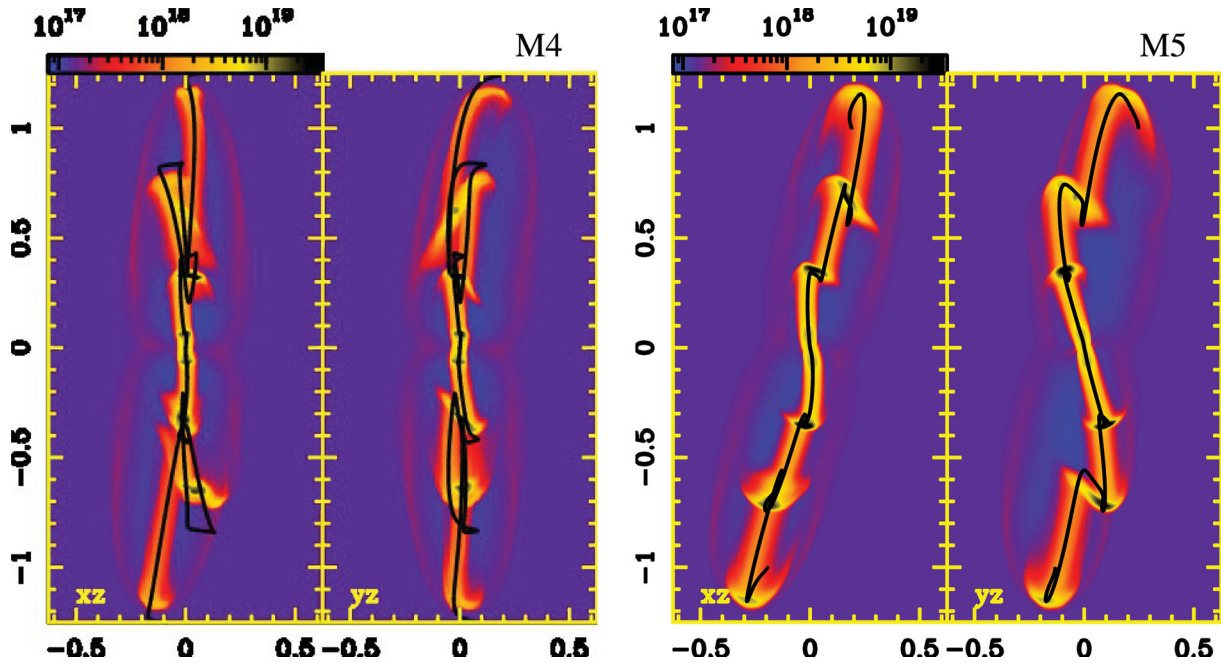


Figure 8. Same as Figs 6 and 7 but left-hand panels showing the column-density maps for model M4, while right-hand panels corresponding to model M5.

The 3D ballistic trajectories obtained from models M2 and M3 are shown in Fig. 3. For model M2, the xz projected trajectory shows a clear point-symmetric quadrupolar morphology, while the yz projection reveals a structure with six lobes. Both projections for model M3 display a quadrupolar morphology, which can be changed by varying the initial phase of the precession motion f_0 (e.g. a six-lobe morphology will be obtained by setting $f_0 = 0$).

In Fig. 4, we compare the projected trajectories on the xz - and yz -planes for model M1c (solid line) and model M1b (dotted line). Both models share the same parameters with the difference that model M1c only has a precession (and no orbital motion). The trajectories obtained from model M1c show a clear global point-symmetric structure. When we include an elliptical orbital motion, a break on this point-symmetric structure is produced, which is clearly observed on the yz -projected trajectories. In these projections, model M1b exhibits a quadrupolar morphology, while the two upper lobes obtained in model M1b become a single upper lobe in model M1c.

The ballistic trajectories obtained for elliptical and circular orbits are compared in Fig. 5 (the projected trajectories for models M1b and M1d are shown with a dashed and a solid line, respectively). Both models show very similar global morphologies.

In order to check the predictions obtained with the semi-analytical calculation, we have also carried out numerical hydrodynamical simulations for all models. After several tests, we found that a good agreement between the numerical simulations and the semi-analytical model is obtained if we consider a ratio between the jet and the environment density greater than 10^3 , as is shown in Figs 6, 7 and 8. These figures display column-density maps (in grey-scale) obtained from numerical simulations of models M1a and M1b (Fig. 6), M2 and M3 (Fig. 7), and M4 and M5 (Fig. 8). The corresponding ballistic trajectories are also shown in black lines, and they trace very well the locus of the jet material obtained from the numerical simulations. Some departures between the numerical simulations and ballistic trajectories are observed in the case of model M4, mainly in the top-right lobe, where the ballistic

trajectory appears ahead of the jet locus obtained from the numerical simulation (see Fig. 7). This departure is produced because the jet gas does not follow a ballistic trajectory when the jet material launched at later times passes through the cocoon generated by the gas emitted at earlier times.

In the previous models, we have considered integer values for the p and q ratios. In models M4 and M5, we explore cases with non-integer p and q values. Fig. 8 shows the column-density maps, in colour scale, obtained from the numerical simulation corresponding to models 4 and 5. The predicted ballistic trajectories of these models are also shown in continuous lines. The xz projection of model M4 resembles the characteristics of the PPN CRL 618 (Riera et al. 2011), while an S-shape is obtained for model M5. This kind of S-shaped morphology is observed in several PPNe and PNe, such as Hen 3-1475 and IC 4634 (Riera, Velázquez & Raga 2004; Guerrero et al. 2008).

5 SUMMARY

We have found that the trajectory of material launched as a precessing and orbiting jet with a time-dependent ejection velocity has a semi-analytical ballistic solution. We find a good fit between this solution and the jet loci obtained through 3D numerical simulations if the initial jet to environment density ratio has a value $\geq 10^3$. The ballistic solution is a good tool for exploring the different parameters which are necessary for modelling specific PPNe, young PNe and HH objects with bipolar or multipolar morphologies.

The obtained results confirm that a morphology with well-defined lobes is obtained if a velocity variability of the precessing and orbiting jet (with a half-amplitude of the order of 50 per cent of the mean jet velocity) is considered (see Figs 2–7). The S-like shapes are generated for slowly precessing jets (i.e. with $p < 1$) as is observed for model M5 in Fig. 8.

This study shows that the effect of the orbital motion is to introduce some departures from the point symmetry due to precession, as is observed in Fig. 4. In addition, the ballistic solution shows that

the differences between trajectories obtained considering circular or elliptical orbital motions are not major (Fig. 5).

We conclude by noting that the semi-analytical ballistic solution (for the trajectory of a precessing and orbiting jet, with a time-dependent ejection velocity) is able to reproduce bipolar, multipolar and ‘S-type’ shapes, all of which are observed in some PPNe and HH objects. These morphologies can be obtained considering different values for the ratio between dynamical time and precession period (our p parameter) and for the ratio between the precession and jet velocity variability periods (our q parameter).

ACKNOWLEDGMENTS

The authors thank Enrique Palacios for maintaining the linux servers where the simulations were performed. PFV, ACR and JC acknowledge support from the CONACyT grants 61547, 101356, 101975, 167611, and UNAM DGAPA grant IN105312. The work of ARI was supported by the MICINN grants AYA2008-06189-C03 and AYA 2011-30228-C03.

REFERENCES

- Bond H. E., Liller W., Mannery E. J., 1978, *ApJ*, 223, 252
 González R. F., Raga A. C., 2004, *Rev. Mex. Astron. Astrofis.*, 40, 61
 Guerrero M. A. et al., 2008, *ApJ*, 683, 272

- Livio M., Salzman J., Shaviv G., 1979, *MNRAS*, 188, 1
 Masciadri E., Raga A. C., 2002, *ApJ*, 568, 733
 Raga A. C., Reipurth B., 2004, *Rev. Mex. Astron. Astrofis.*, 40, 15
 Raga A. C., Navarro-González R., Villagrán-Muniz M., 2000, *Rev. Mex. Astron. Astrofis.*, 36, 67
 Raga A. C., Esquivel A., Velázquez P. F., Cantó J., Haro-Corzo S., Riera A., Rodríguez-González A., 2009, *ApJ*, 707, L6
 Riera A., Velázquez P. F., Raga A. C., 2004, in Meixner M., Kastner J. H., Balick B., Soker N., eds, *ASP Conf. Ser. Vol. 313, Asymmetrical Planetary Nebulae III: Winds, Structure and the Thunderbird*. Astron. Soc. Pac., San Francisco, p. 487
 Riera A., Raga A. C., Velázquez P. F., Haro-Corzo S. A. R., Kajdic P., 2011, *A&A*, 533, A118
 Soker N., Livio M., 1994, *ApJ*, 421, 219
 Terquem C., Eislöffel J., Papaloizou J. C. B., Nelson R. P., 1999, *ApJ*, 512, L131
 van Leer B., 1982, in Krause E., ed., *Lecture Notes in Physics, Vol. 170, Numerical Methods in Fluid Dynamics*. Springer, Berlin, p. 507
 Velázquez P. F., Steffen W., Raga A. C., Haro-Corzo S., Esquivel A., Cantó J., Riera A., 2011, *ApJ*, 734, 57
 Velázquez P. F., Raga A. C., Riera A., Steffen W., Esquivel A., Cantó J., Haro-Corzo S., 2012, *MNRAS*, 419, 3529
 Witt A. N., Vijh U. P., Hobbs L. M., Aufdenberg J. P., Thorburn J. A., York D. G., 2009, *ApJ*, 693, 1946

This paper has been typeset from a $\text{\TeX}/\text{\LaTeX}$ file prepared by the author.